Acta Oceanol. Sin., 2021, Vol. 40, No. 10, P. 17–29
https://doi.org/10.1007/s13131-021-1770-x
http://www.aosocean.com
E-mail: ocean2@hyxb.org.cn

Three-dimensional properties of mesoscale cyclonic warm-core and anticyclonic cold-core eddies in the South China Sea

Wenjin Sun[1, 2], Yu Liu[2, 3], Gengxin Chen[4], Wei Tan[5], Xiayan Lin[3], Yuping Guan[4, 6], Changming Dong[1, 2*]

[1] School of Marine Sciences, Nanjing University of Information Science and Technology, Nanjing 210044, China

[2] Southern Marine Science and Engineering Guangdong Laboratory (Zhuhai), Zhuhai 519080, China

[3] Marine Science and Technology College, Zhejiang Ocean University, Zhoushan 316022, China

[4] State Key Laboratory of Tropical Oceanography, South China Sea Institute of Oceanology, Chinese Academy of Sciences, Guangzhou 510301, China

[5] College of Ocean Science and Engineering, Shandong University of Science and Technology, Qingdao 266590, China

[6] College of Earth and Planetary Sciences, University of Chinese Academy of Sciences, Beijing 100049, China

Received 31 October 2020; accepted 28 December 2020

Abstract

In general, a mesoscale cyclonic (anticyclonic) eddy has a colder (warmer) core, and it is considered as a cold (warm) eddy. However, recently research found that there are a number of "abnormal" mesoscale cyclonic (anticyclonic) eddies associated with warm (cold) cores in the South China Sea (SCS). These "abnormal" eddies pose a challenge to previous works on eddy detection, characteristic analysis, eddy-induced heat and salt transports, and even on mesoscale eddy dynamics. Based on a 9-year (2000–2008) numerical modelling data, the cyclonic warm-core eddies (CWEs) and anticyclonic cold-core eddies (ACEs) in the SCS are analyzed. This study found that the highest incidence area of the "abnormal" eddies is the northwest of Luzon Strait. In terms of the eddy snapshot counting method, 8 620 CWEs and 9 879 ACEs are detected, accounting for 14.6% and 15.8% of the total eddy number, respectively. The size of the "abnormal" eddies is usually smaller than that of the "normal" eddies, with the radius only around 50 km. In the generation time aspect, they usually appear within the 0.1–0.3 interval in the normalized eddy lifespan. The survival time of CWEs (ACEs) occupies 16.3% (17.1%) of the total eddy lifespan. Based on two case studies, the intrusion of Kuroshio warm water is considered as a key mechanism for the generation of these "abnormal" eddies near the northeastern SCS.

Key words: mesoscale eddy, cyclonic warm-core eddy, anticyclonic cold-core eddy, Kuroshio intrusion, South China Sea, abnormal mesoscale eddy

Citation: Sun Wenjin, Liu Yu, Chen Gengxin, Tan Wei, Lin Xiayan, Guan Yuping, Dong Changming. 2021. Three-dimensional properties of mesoscale cyclonic warm-core and anticyclonic cold-core eddies in the South China Sea. Acta Oceanologica Sinica, 40(10): 17–29, doi: 10.1007/s13131-021-1770-x

1 Introduction

The South China Sea (SCS) is the deepest and largest semi-closed marginal sea in the northwestern Pacific Ocean (Fig. 1). Its northern, western and southern boundaries are land, and it is separated from the Pacific Ocean by the Philippine Islands and Taiwan Island in the east. The SCS is connected to the Sulu Sea, the Indian Ocean and the Pacific Ocean through the Mindoro Strait, Malacca Strait and Luzon Strait, respectively. Several previous literature points out that the SCS is a hotspot for energetic mesoscale eddy activities. Their research refers to eddy statistical characteristic (Wang et al., 2003, 2015a, 2019a; Zhang et al., 2018; He et al., 2018), eddy case study (Nan et al., 2011; Chu et al., 2014; Wang et al., 2015b; Qiu et al., 2019a, 2019b), eddy–mean flow interaction (Zhong et al., 2016; Su et al., 2020), eddy-induced variations of oceanic and atmospheric physical parameters (Xian et al., 2012; Zhang et al., 2015; Liu et al., 2017b; Yang et al., 2017; Li et al., 2018), eddy formation mechanisms (Yang et al., 2013; Qiu et al., 2020), among others (Wang et al., 2020).

There are 32.9±2.4 eddies identified from numerical modelling data in terms of the surface characteristic aspect, and

Foundation item: The National Natural Science Foundation of China under contract Nos 41906008, 41806039, 41806030, 42076021, 41676010 and 41706205; the State Key Laboratory of Tropical Oceanography, South China Sea Institute of Oceanology, Chinese Academy of Sciences under contract Nos LTO1902 and LTO1807; the Strategic Priority Research Program of Chinese Academy of Sciences under contract No. XDB42000000; the Youth Innovation Promotion Association CAS under contract No. 2017397; the Pearl River S&T Nova Program of Guangzhou under contract No. 201806010105; the Open Fund of State Key Laboratory of Satellite Ocean Environment Dynamics, Second Institute of Oceanography, MNR under contract No. QNHX2022; the Startup Foundation for Introducing Talent of Nanjing University of Information Science & Technology under contract No. 2019r049; the Startup Foundation for Introducing Talent of Zhejiang Ocean University; the National Key Research Programs of China under contract Nos 2016YFC1401407 and 2017YFA0604100; the National Programme on Global Change and Air-Sea Interaction under contract Nos GASI-IPOVAI-03 and GASI-IPOVAI-05; the Innovation Group Project of Southern Marine Science and Engineering Guangdong Laboratory (Zhuhai) under contract No. 311020004.

*Corresponding author, E-mail: cmdong@nuist.edu.cn

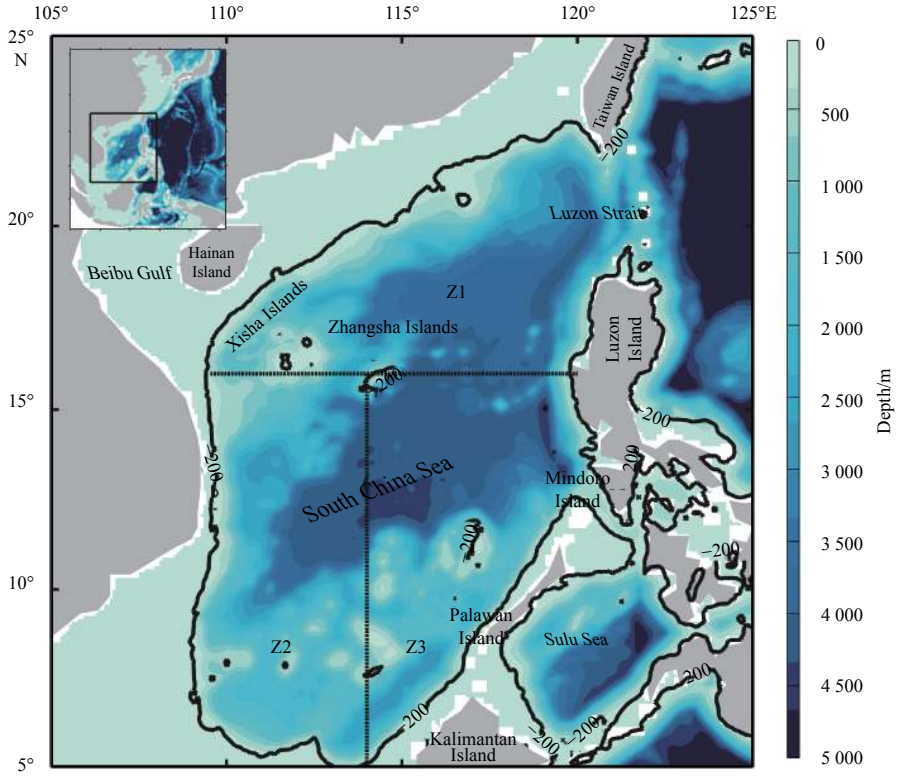

Fig. 1. Topography of the South China Sea. Shading indicates water depth (unit: m) and the black contour represents the 200 m isobath. The dashed lines are the boundaries of the subregions: Z1, Z2 and Z3, indicating the northern SCS, southwestern SCS, and southeastern SCS, respectively.

32.8±3.4 eddies identified from satellite altimeter data in each year from 1993 to 2007 in the SCS (Xiu et al., 2010). The average radius is 87.4 km. For about 30% of these eddies, the radius is even larger than 100 km. The average lifespan is 8.8 weeks (Chen et al., 2011). The translational velocity is about 0.1 m/s (Wu and Chiang, 2007). In terms of spatial distribution, these eddies are mainly concentrated in a northeast–southwest oriented belt along the continental slope and southwest of Luzon Island (Chen et al., 2012).

Some scholars have also studied the three-dimensional structure of mesoscale eddies in the SCS. For instance, based on multiple observation data, Hu et al. (2011) analyze a cyclonic eddy (CE) off the Vietnam Coast, and they demonstrate that the eddy center axis is tilted southwestward with depth. Using the South China Sea Mesoscale Eddy Experiment data, Zhang et al. (2016) obtain similar results. Based on numerical simulation data, Lin et al. (2015) reveal three different eddy structures (bowl-shaped, lens-shaped and cone-shaped) in the SCS. Combining satellite altimeter and Argo profiles data, Sun et al. (2018) find that both of the composited CEs and anticyclonic eddies (AEs) are bowl-shaped and have a thickness of about 400 m, and this result is also supported by He et al. (2018).

Influenced by CEs, the thermocline becomes shallower/thinner with strengthened intensity/gradient, while the effects are opposite for anticyclonic eddies (Chen et al., 2011). Eddies can transport heat, salt, freshwater, and biogeochemical substances as well (Chelton et al., 2011; Zhang et al., 2014a, b; He et al., 2016; Xu et al., 2014, 2016; Wang et al., 2018). Besides, the eddy-induced sea surface temperature (SST) perturbations can impact the atmosphere (Ma et al., 2015; Byrne et al., 2016). Previous studies have shown that the surface wind curl input (Chi et al., 1998; Hu et al., 2000; Qu, 2000), current interaction with complex bottom topography (Chen et al., 2015) and Kuroshio intrusion (Zhang et al., 2017; Yang et al., 2019) are three major factors in eddy generation in the SCS.

These previous studies have laid a solid foundation for the understanding of mesoscale eddies in the SCS. However, most of these studies aimed at “normal” eddies, i.e., cyclonic cold-core eddies and anticyclonic warm-core eddies. Recently, Sun et al. (2019) found a number of mesoscale cyclonic (anticyclonic) eddies associated with warm (cold) cores in the SCS. Different from the conventional or normal eddies, these cyclonic warm-core eddies (CWEs) and anticyclonic cold-core eddies (ACEs) are defined as “abnormal” eddies in this study (for a strict definition, please see Section 2.3).

The cyclonic warm-core and anticyclonic cold-core eddies (CW-ACEs) are rarely, compared with the “normal” eddies. Only a few studies discussed them in other areas (Yasuda et al., 2000; Rogachev, 2000; Mathis et al., 2007; Itoh and Yasuda, 2010a, 2010b; Ji et al., 2017). Four “abnormal” eddy generation mechanisms are mentioned in previous studies. (1) ACEs are generated by strong mixing. Martin and Richards (2001) emphasized the role of mode water created by winter mixing in the generation of ACEs; (2) ACEs are generated by the interaction between water masses in special areas, e.g., AEs in the Bussol’ Strait are strengthened by the supply from the Okhotsk Sea’s cold and fresh water (Yasuda et al., 2000; Rabinovich et al., 2002), or CEs change polarity to form ACEs (Martin and Richards, 2001); (3) CW-ACEs are generated by various instability processes (Pickart et al., 2005; Spall et al., 2008; Kadko et al., 2008). Due to a sudden increase of the eddy radius, a “normal” CE can absorb warm waters from the surrounding area, and finally turn into a CWE during its decay-

ing stage (Sun et al., 2019); (4) CW-ACEs are generated by upwelling/downwelling processes driven by eddy–wind interaction. The upwelling in "normal" AEs can form ACEs, and the downwelling in "normal" CEs can produce CWEs (McGillicuddy, 2015).

In the SCS, there are only a few researches on "abnormal" eddies has been reported. Their spatial distribution, number, size, generation time, survival time, three-dimensional structure, and generation mechanism are still unclear. The solution to these problems is crucial to deepen our understanding of the mesoscale eddy diversity, accurately quantifying the eddy-induced heat and salt transports and a series of other scientific problems. Therefore, the details of the CW-ACEs in the SCS are discussed in this study.

The rest of the article is organized as follows. Section 2 describes the numerical modelling output data, eddy detection and tracking method, and the strict definition of the "abnormal" eddy. Two "abnormal" cases are illustrated in Section 3. Section 4 is about the general statistical characteristics (spatial distribution, number, size, generation time and survival time) of the "abnormal" eddies. Section 5 discusses the possible generation mechanism of the CW-ACEs based on two cases shown in Section 3. The conclusions are provided in Section 6.

2 Data and methods

2.1 *Model output data*

The Regional Ocean Modelling System (ROMS, Roms_Agrif_v2.1) output from Lin et al. (2015) is used in this study. ROMS employs the curvilinear and sigma coordinate in the horizontal and vertical directions, respectively (Shchepetkin and McWilliams, 2003). The model domain is (9°S–41°N, 99°–145.5°E) and covers the whole SCS. Its horizontal resolution is (1/12)° by (1/12)°. There are 32 layers in the vertical direction, and the K-profile parameterization scheme (Large et al., 1994) is applied for the vertical eddy viscosity. Velocity, potential temperature, salinity, and sea surface height from the Simple Ocean Data Assimilation are used to initialize the model. This data has a resolution of 0.5° by 0.5°. The model is first spin-up for 10 years (1948–1957), forced by the surface fluxes from the weekly NCEP/NCAR reanalysis 1 (Kalnay et al., 1996). Afterwards, the daily wind stress forcing from NCEP/NCAR reanalysis 1 is added from January 1958 to July 1999, and from August 1999 to December 2008 with forcing from the daily blended sea winds (Zhang et al., 2006). Daily model output during the last 9 years (2000–2008) is used to study the "abnormal" eddies in the SCS (5°–23°N, 108°–121°E). Also, only the area deeper than 200 m (black contour in Fig. 1) is chosen as the research area. Considering complex dynamics in the SCS, the "abnormal" eddies may be region-dependent. The SCS is, therefore, further separated into three subregions for detailed analysis (Chen et al., 2011): northern SCS (Z1, 16°–23°N, 108°–121°E), southwestern SCS (Z2, 5°–16°N, 108°–114°E) and southeastern SCS (Z3, 5°–16°N, 114°–121°E). For a detailed description of the model configuration, please refer to Lin et al. (2015). The model configuration files can be downloaded from http://doi.org/10.528 1/zenodo.3533930.

Lin et al. (2015) passed this numerical modelling data through a series of verification processes. These validation results are briefly described below. Firstly, the seasonal flow field in the SCS derived from the sea surface height anomalies observed by satellite altimeter data is very similar to the simulation. In summer, a large anticyclonic gyre off the coast of Vietnam and a re-circulation of the northward coastal jet along Vietnam and Hainan Island are observed in both satellite and model data. Similar conditions in winter, with two congruous cyclonic gyres, are also obtained. Secondly, the simulated SST anomalies (removing the annual mean temperature) also correspond well to the observed SST anomalies from advanced very high resolution radiometer (AVHRR). Thirdly, the normalized SST averaged in the whole SCS shows the same seasonal variation with AVHRR data during 2000–2008. Fourthly, the intra-seasonal eddy kinetic energy (90-day high-pass filtering) is similar between the observed and simulated results, in both spatial distribution patterns and local characteristics. In summary, this model data can accurately reproduce the observed seasonal and intra-seasonal variations in the SCS, and can be used here for mesoscale eddy research.

2.2 *Eddy detection and tracking method*

For the convenience of eddy detection and analysis, this study first linearly interpolates every physical parameter onto 15 vertical levels (10 m, 50 m, 100 m, 150 m, 200 m, 250 m, 300 m, 350 m, 400 m, 450 m, 500 m, 550 m, 600 m, 650 m and 700 m). Considering that the average depth of the mesoscale eddies in the SCS is about 400 m (He et al., 2018), a 700-m depth is enough for analysis. At each level, the vector geometry method (Nencioli et al., 2010) is used to obtain the two-dimensional eddy information. This method has been successfully applied to eddy detection from satellite observation data (Liu et al., 2012; Dong et al., 2014; Sun et al., 2017; Yang et al., 2020) and numerical model output data (Dong et al., 2012; Liu et al., 2017a; Wang et al., 2019b). This method includes three main steps.

Step 1: determining the two-dimensional eddy center based on the following four constraints. First (Second), along the meridional (zonal) section, the zonal (meridional) velocity u (v) has opposite signs on the northern and southern (eastern and western) sides of the eddy center, and its magnitude gradually increases within "a" grid points away from the eddy center. Third, at the eddy center, the magnitude of the velocity is the local minimum within a region extending from the center to "b" grid points away. Fourth, along "$a-1$" grid points from the center, the velocity vectors present a clockwise or an anticlockwise rotation. Here, the two parameters "a" and "b" are set to "$a=3$" and "$b=2$".

Step 2: extracting the outermost enclosed contour of local stream function around the eddy center as the two-dimensional eddy boundary.

Step 3: tracking the two-dimensional eddy following the method proposed by Doglioli et al. (2007) and Chaigneau et al. (2008). This study first sets a suitable searching area (a circular region centered around the eddy center) and an expanded searching area (1.5 times the radius of the searching area). Assuming an eddy is successfully detected at time step t, it can be tracked as the nearest consistent polarity eddy center at time step $t+1$ within the searching area. In order to avoid the possibility that one single eddy is tracked as two or more eddies, an extra search is conducted at time step $t+2$ within the expanded searching area. If no eddy centers satisfying the above conditions are detected at time step $t+2$, this eddy is considered dissipated and its lifespan ends at time step t. Otherwise, if more than one eddy center satisfies the above conditions at time step $t+2$, this eddy is considered as still "existing", and the nearest eddy is regarded as a continuum of the eddy at time step t.

In order to analyze the three-dimensional structures of the CW-ACEs, the three-dimensional eddy detection method developed by Lin et al. (2015) is used in this study as well. This method integrates the discrete eddy information into three-di-

mension information based on the two-dimensional plane detection results. Considering the eddy center axis may be tilted in the vertical direction (Hu et al., 2011; Zhang et al., 2016), the upper and lower eddy centers may be not located in the same plane position. This method assumes that the same eddy on the upper and lower layers have the same occurrence time and polarity. Besides, the drift of the eddy center is assumed to be less than a quarter of its radius between two neighboring levels. By following this scheme, the centers are vertically searched from the surface (10 m) to 700 m within a defined searching area (a quarter of its radius). The search is iterated downward until the target eddy cannot be found at the next level. Finally, a three-dimensional eddy dataset is produced, which contains the eddy polarity, occurrence time, vertical penetration depth, radius, eddy center location and horizontal boundary at each level.

To make the results more meaningful, this study proposes three screening conditions for the results obtained from automated eddy detection process. Firstly, considering that the characteristic time scale of the mesoscale eddies is in month, only the eddies surviving for more than 10 days are selected. Secondly, since the spatial scale of the mesoscale eddies is O (100 km) and the model resolution is (1/12)° by (1/12)°, only the eddies with an average radius of larger than 20 km are used. Thirdly, to make the eddy more representative, only the eddies of which the vertical penetration depth is deeper than 100 m is selected.

2.3 *Definition of "abnormal" eddies*

Eddies satisfying the following criteria are defined as "abnormal" eddies. (1) The eddy is determined at a certain vertical level (regardless of the eddy lifespan), the absolute value of average potential temperature difference (θ') between the eddy ($\theta_{\rm in}$) and the background area ($\theta_{\rm bc}$) must be larger than a critical value (α). That is, for the CWE, $\theta_{\rm in} - \theta_{\rm bc} > \alpha$, and for the ACE, $\theta_{\rm in} - \theta_{\rm bc} < \alpha$. In this study, the critical value is defined as zero. Different critical values will give different results, especially the number of "abnormal" eddies. However, based on the test results, different critical value will not impact the results substantially. Here, the background area is defined as an annular region between the eddy boundary (dashed circle in Fig. 2) and the circle with radius 1.5 times the radius of the eddy (solid circle in Fig. 2). If a CE or AE satisfies the above criterion at any vertical level, it is considered as a CWE or an ACE. By considering the sensitivity of different background area sizes, this study also uses 2 times the eddy radius as the background area. The results present no significant difference (not shown). The "abnormal" eddies detected above are all based on snapshots, therefore, the eddy lifespan is not considered. (2) When considering an eddy with a lifespan, an "abnormal" eddy is defined as long as there is a time point in its lifetime that satisfies condition 1.

3 Three-dimensional structure of two cases

The three-dimensional structure of a CWE at the depths of 20 m, 100 m, 300 m, and 400 m is illustrated in Fig. 2a. In this snapshot (August 12, 2006), the eddy surface center is located at 20.5°N and 119.7°E. This CWE is a drop-shaped in horizontal direction and a bowl-shaped in vertical direction. Its average radius is 40.6 km at the eddy surface (10 m), and decreases to 26.8 km at the eddy bottom (400 m). The gradual attenuation of the eddy radius is

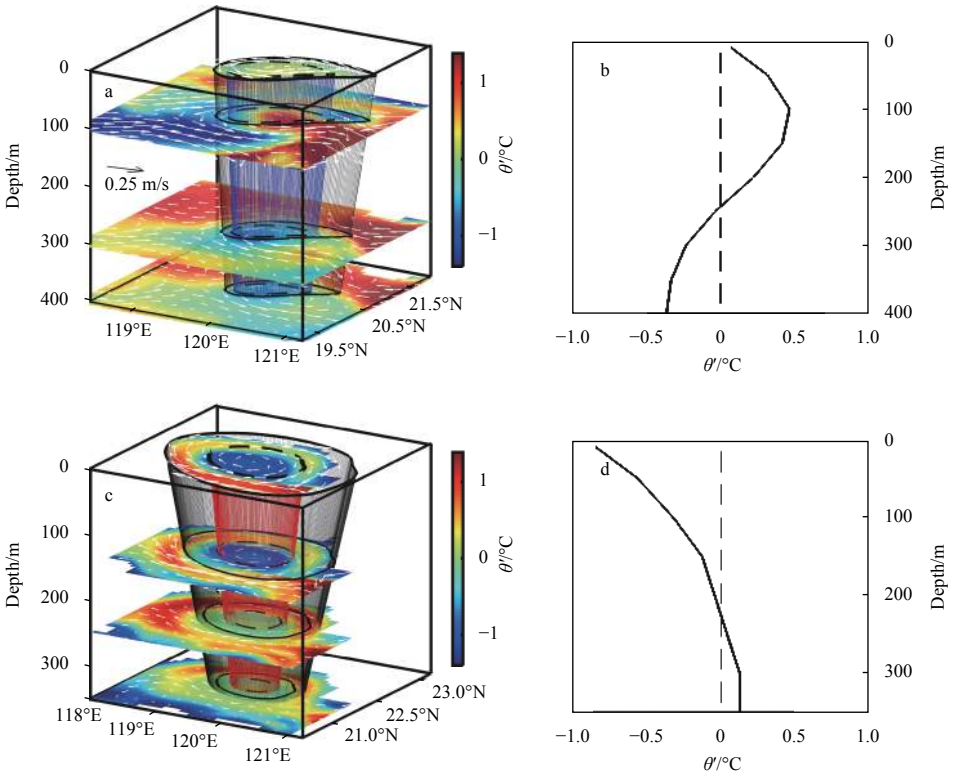

Fig. 2. Three-dimensional structures of the CWE (a) and ACE (c). Colors denote potential temperature anomalies (θ', unit: °C) and white vectors indicate horizontal velocity anomalies (unit: m/s). The blue/red outlines are the eddy boundaries (outermost enclosed contour of local stream function around the eddy center) and also mark the background area's inner boundaries. The grey outlines mark the outer background boundaries (1.5 times the radius of the eddy). The vertical profiles of θ' (b, d) are calculated within the same eddies as shown in a and c.

consistent with previous results based on composite analyses (Zhang et al., 2013; Sun et al., 2018; He et al., 2018). There is a warm core in the upper 250 m and a cold-core in deeper layers (Fig. 2b). The largest θ' is 0.5°C occurring at around 100 m. The CWE cannot keep its surface warm-core characteristic as it penetrates downward. That is, this "abnormal" phenomenon only exists at some certain depths. There are two possible factors contributing to this phenomenon. One is the fact that the upper warm water is less dense than the lower cold water, forming a stable stratification. The other one is the divergent effect of the cyclonic eddy, which can bring deep cold water to the upper layers through upwelling. Both of them are unfavorable for the downward transport of the warm water, thus the warm water inside the "abnormal" eddy is concentrated in the upper layer.

The three-dimensional structure of an ACE at the depths of 10 m, 150 m, 250 m, and 350 m is illustrated in Fig. 2c. This ACE snapshot appears to the northwest of Luzon Strait (21.7°N, 119.5°E) on January 2, 2000. Its horizontal shape is close to a circle, and is more regular than the CWE (Fig. 2a). In addition, the penetration depth of the ACE (350 m) is slightly shallower than that of the CWE (400 m). The mean eddy radius decreases with depth as well. It is 65.5 km at the surface (10 m), and decreases to 32.7 km at the eddy bottom (350 m). This ACE has a cold core in the upper 250 m and a warm core in the deeper layers (Fig. 2d). The maximum θ' (–0.8°C) occurs at the surface layer (10 m) and then gradually decreases with depth until θ' changes its sign at 250 m. The anomalous ACE is also concentrated in the upper layer. Summarizing above these two cases, the "abnormal" phenomenon mainly occurs in the upper part of the eddy, while it remains "normal" in the lower part.

Statistics show that the average depth of the "abnormal" θ' associated with CWEs and ACEs is 40.8 m and 40.5 m, respectively. It is a little deeper than the local mixed layer depth (33.1 m), which is defined as the depth with a temperature 0.5°C lower than the surface temperature. The depth of the "abnormal" θ' for both CWEs and ACEs shows a seasonal variation in the SCS, which is deeper in winter, and shallower in summer (not shown). This is consistent with the mixed layer depth, implying a possible modulation of the climatological background.

4 Eddy basic characteristics

4.1 *Eddy spatial distribution*

The spatial distribution of CW-ACEs in 1° by 1° bins is presented in Fig. 3 (based on the eddy snapshot counting method). Unlike the "normal" eddies (Chen et al., 2011), the maximum number of the "abnormal" eddies appears to the northwest of the Luzon Strait (151 CWEs, and 277 ACEs). This may be associated with the Kuroshio intrusion which can lead to the exchange of water masses with significantly different properties. There are also some other high-occurrence areas, such as the marginal shallow waters of the SCS and the southwest region of Luzon Island. This may be related to the shallow water depth with strong interactions between eddies and the surrounding topography. This question is beyond the scope of this study, and deserves further analysis in the future.

4.2 *Eddy number*

Two methods are used to calculate the number of eddies: eddy snapshot counting (ESC) method and eddy lifespan counting (ELC) method. In the ESC method, an eddy snapshot is considered as one eddy without regard to its lifespan. That is, an eddy which lives N days is denoted as N eddies. Using this method, 8 620 CWEs and 9 879 ACEs are detected in the SCS from January 1, 2000 to December 31, 2008, corresponding to 14.6% and 15.8% of the total eddies. If the criterion α is raised to 0.1°C, then the proportion decreases to 4.3% and 5.2%, respectively. The number of CWEs is less than that of ACEs, which is consistent with Chen et al. (2011).

As for the ELC method, the whole eddy lifespan is considered as one eddy. That is, an eddy that lives N days is only regarded as one eddy. Using the ELC method, there are 1 087 CWEs and 914 ACEs in the same period, corresponding to 18.5% and 14.6% of the total eddies. Compared with the ESC method, the number of

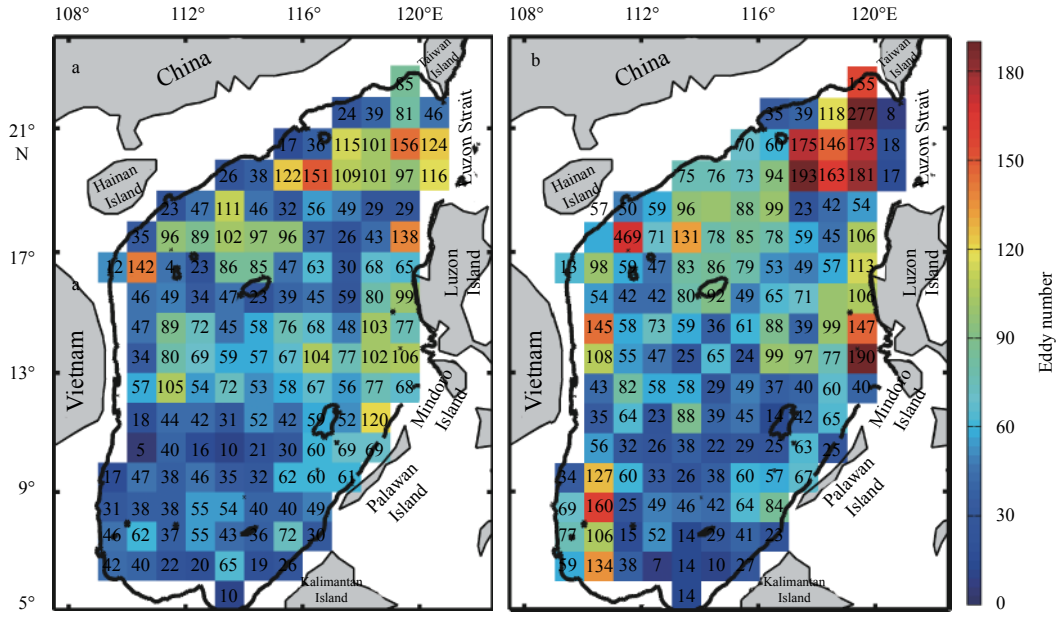

Fig. 3. Number of the CWEs (a) and ACEs (b) in 1° by 1° bins in the SCS. The number of eddies in each bin are also represented by the colors. The black contour represents the 200 m isobath.

CWEs is slightly more than that of ACEs. It indicates that the survival time of ACEs is longer than that of CWEs. After the CWE forms, the bottom cold water is continuously transported upward due to the eddy-induced upwelling, and thus mixes with the upper warm water. Therefore, the CWE is difficult to survive for a long time. On the contrary, the ACE corresponds to downwelling, the upper "abnormal" cold water is transported downward, and mixes with the cold water in the lower layer, as a consequence, the ACE can survive for a relatively longer time.

To obtain the vertical distribution of the "abnormal" eddies, the number of CW-ACEs in the whole SCS is counted separately at the 15 vertical levels (based on the ESC method; Fig. 4). The most unique feature is that the number of eddies decreases exponentially with depth in the upper 300 m, and becomes very small below 300 m. For both CWEs and ACEs, the number at 50 m is only half of that at the surface (10 m). This distribution characteristic can be inferred from the case analysis in Section 3 as well. The "abnormal" phenomenon usually concentrates in the upper layers of the eddies, thus the number of eddies decreases with the depth as a matter of course. Another noteworthy feature is that the relative numbers of CWEs and ACEs change at 200 m. In the upper 200 m, the ACEs are more than CWEs, but in the lower depth, the relation reverses (Fig. 4a). The reverse-depth varies in different subregions of the SCS. It is 400 m in the northern SCS (Fig. 4b), and 100 m in the southwestern SCS (Fig. 4c). In the southeastern SCS, however, the CWEs are always more than ACEs in all the 15 levels, despite a small difference (Fig. 4d). Different dynamic environments may cause this regional difference (Chen et al., 2011; Sun et al., 2018). The reverse relationship of the relative number also exists in "normal" eddies, and the reverse-depth of the "normal" eddies is much deeper, about 400 m (Lin et al., 2015).

4.3 *Eddy radius*

For the two "abnormal" cases in Section 3, the radius gradually decreases with depth (Figs 2a and c). In order to gain a more general understanding, the average radius of the "abnormal" eddy with respect to depth is shown in Fig. 5. In the whole SCS, the maximum radius appears at 50 m, and the average eddy radius decreases gradually from 50 m to 700 m as expected (Fig. 5a). Generally, the average radius of ACEs is larger than that of CWEs at each level. More precisely, the average radius of CWEs (ACEs) is (66.0±0.6) km ((68.9±0.5) km) (average±standard error) at 50 m, (55.6±0.7) km ((61.9±0.8) km) at 400 m and (48.4±0.7) km ((53.3±1.3) km) at 700 m (Fig. 5a). Similar patterns can be found in the northern SCS, except that the maximum radius of ACEs is at 300 m instead of 50 m (Fig. 5b). In the southwestern SCS (Fig. 5c) and southeastern SCS (Fig. 5d), the differences of the average radius between CWEs and ACEs are relatively small. The radius of "abnormal" eddies tends to decrease with depth. This is observed from the average of the whole SCS and from the average of the three local subregions.

The horizontal distribution of the "abnormal" eddy radius at 10 m, 100 m, 200 m and 300 m are given in Fig. 6. The largest eddy radius appears to the southeast of Vietnam in the upper 100 m (Figs 6a, b, e and f), which is different from the eddy numbers (Fig. 3). Below 200 m, the region with the largest eddy radius gradually moves toward the central basin (Figs 6c, d, g and h). This is consistent with all the eddies, or "normal" eddies in the

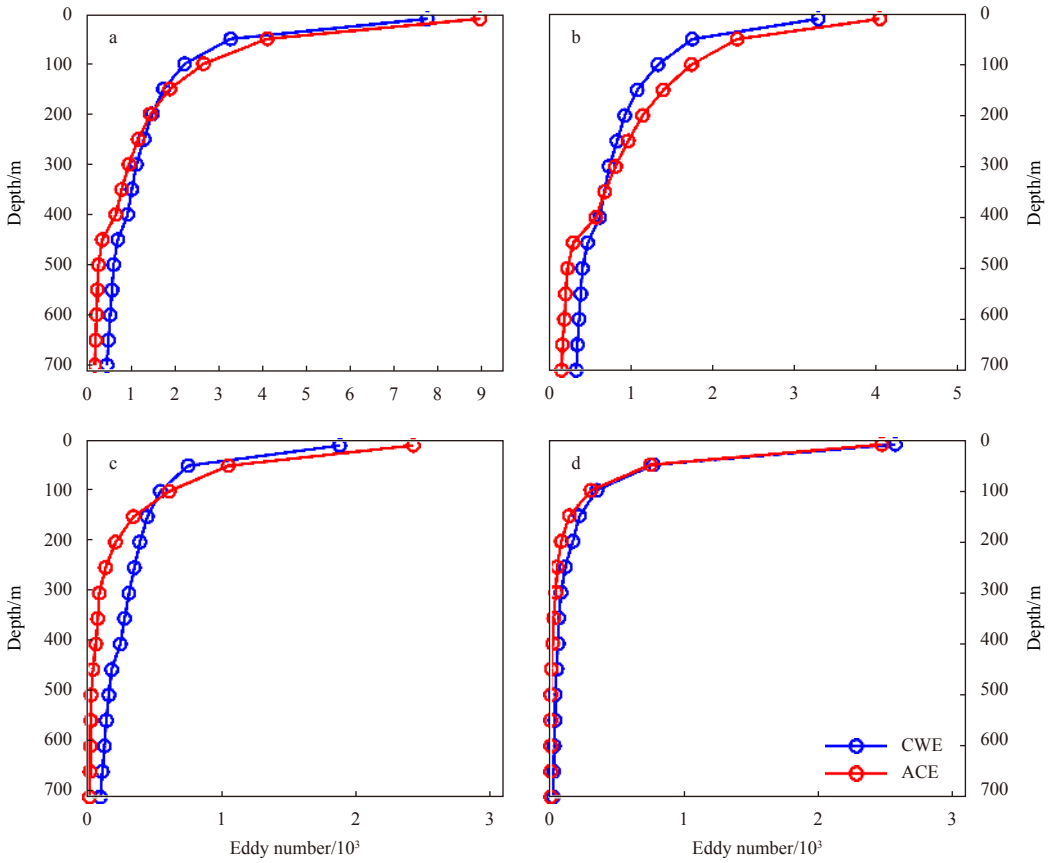

Fig. 4. Vertical distributions of the number of CWEs (blue line) and ACEs (red line) from January 1, 2000 to December 31, 2008 in the whole SCS (a), northern SCS (b), southwestern SCS (c), and southeastern SCS (d).

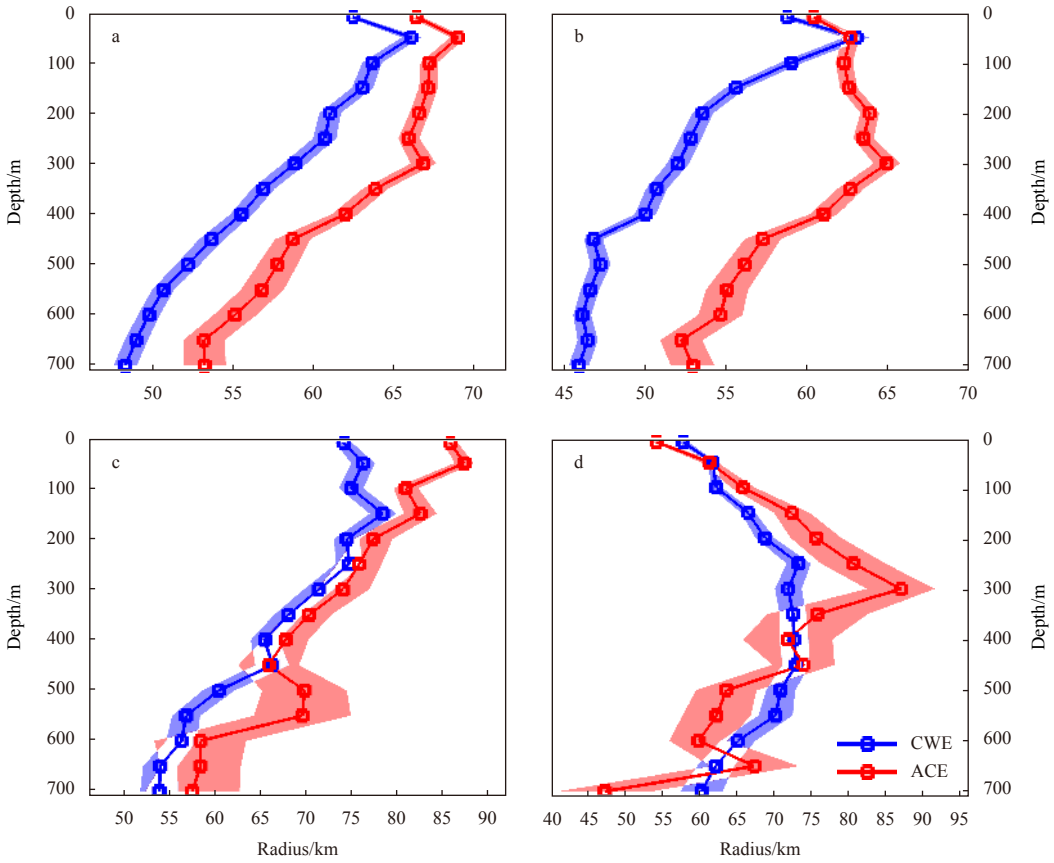

Fig. 5. Vertical profiles of the average radius (unit: km) of CWEs (blue line) and ACEs (red line) in the whole SCS (a), northern SCS (b), southwestern SCS (c), and southeastern SCS (d). The shading indicates the standard error, defined as $\pm\frac{\sigma(z)}{\sqrt{N(z)}}$, where $\sigma(z)$ is the standard deviation and $N(z)$ is the corresponding eddy number at z level.

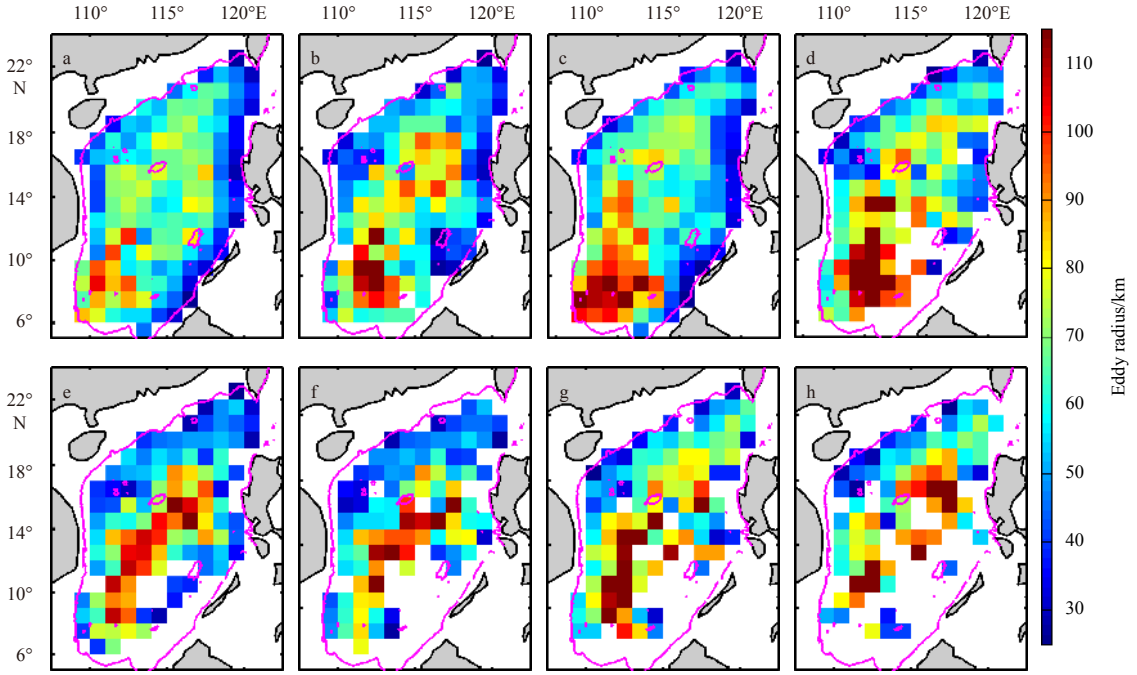

Fig. 6. Average radius (unit: km) of CWEs and ACEs at 10 m (a, e), 100 m (b, f), 200 m (c, g) and 300 m (d, h). a–d are for CWEs and e–h are for ACEs. The magenta curves represent the 200 m isobath.

SCS (Lin et al., 2015). This spatial distribution can be understood from two aspects. One is related to the topography. In the shallow sea of the continental shelf and near islands, the development of eddy is restricted by the bottom and lateral boundary, leading to small eddy radius. While in the central SCS, the eddy has more space for development. The other possible reason is that most eddies in the central SCS are in the "mature" stage, when the eddy radius is naturally larger than that in other stages.

4.4 *Eddy generation time*

Generally, an eddy does not always keep "abnormal" state during its whole lifespan (Sun et al., 2019). Therefore, the question is: at which stage do "normal" eddies change to "abnormal" eddies? To solve this question, the annual average numbers of CW-ACEs in different normalized life stages are quantified (Fig. 7). Remarkably, most of the CW-ACEs exist in the 0.1–0.3 stage of the normalized lifespan, which indicates that CW-ACEs mainly occur in the "youth stage". This is because that the eddy is unstable in the "youth stage" and is more susceptible to the influence of the surrounding water. Thus, the eddy is prone to generate the abnormal phenomena. This characteristic is captured in all the three subregions (Figs 7b–d), indicating a less regional dependence. Besides, ACEs are more than CWEs in most of the stages (Figs 7a–c), except in the southeastern SCS after 0.4 stage (Fig. 7d), this is determined by the fact that there are more ACEs than CWEs (Section 4.2).

4.5 *Eddy survival time*

Previous studies demonstrate that CEs and AEs can change to CWEs and ACEs, and vice versa (Sun et al., 2019). The survival time of the CWE/ACE is defined as the sum of all the days during which the CWE/ACE exists in this study. For example, if a CE (AE) survives for N days and has a warm-core (cold-core) center for M days ($M \leqslant N$), then the survival time of the CWE (ACE) is defined as M days. The histogram of the survival time and corresponding ratio of the "abnormal" time-length (γ) are given in Fig. 8. Here, γ is defined as the ratio of M to N, i.e., $\gamma = \dfrac{M}{N} \times 100\%$.

Compared with the "normal" eddies, the survival time of both CWEs and ACEs are much shorter (Fig. 8). Most "abnormal" eddies survive only 5–10 d (Figs 8a, c, e and g). In the whole SCS, the average survival times are (7.8±0.3) d (mean±standard error) and (10.8±0.9) d for CWEs and ACEs, respectively (Fig. 8a). While for all the CEs (AEs) in the SCS, the average lifespan is 48 (63) d based on the same data (Lin et al., 2015). Consequently, the survival time of the CWEs (ACEs) accounts for about 16.3% (17.1%) of the total eddy lifespan. Only a few "abnormal" eddies can persist throughout the whole lifespan. In most cases, the CW-ACEs phenomena are just a transient state of the "normal" eddies. Similar to the generation time, the survival time and corresponding ratio of "abnormal" eddies also have less regional dependence (Figs 8b, d, f and h). Besides, the strength of "abnormal" eddies is usually smaller than that of "normal" eddies. Comparison of the results from He et al. (2018) shows that the temperature and salinity changes induced by "abnormal" eddies are only about 10 % of those caused by "normal" eddies (not shown).

5 Discussion

Previous research in the Bussol' Strait point out that these "abnormal" eddies are related to the special water mass around them (Yasuda et al., 2000; Rabinovich et al., 2002). In the SCS, the CW-ACEs mainly appear to the northwest of the Luzon Strait (Fig. 3). Therefore, it can be reasonably inferred that the CW-ACEs in the northeastern SCS are related to the Kuroshio intrusion. In order to verify the rationality of this inference, two cases (a CWE case surviving from August 11, 2006 to September 15, 2006, and an ACE case from January 1, 2000 to January 17, 2000) are selected to discuss this problem in details.

For the CWE case, the eddy grows in the "youth stage", maintains its stability in the "mature stage" and gradually decays in the "aged stage" (Fig. 9a). The average surface eddy radius during the whole lifespan is 45.5 km. This eddy almost exhibits CWE characteristic during its whole lifespan, except at its formation stage (Fig. 9b).

To understand the evolution of this CWE, the surface velocity and SST on the 3rd, 17th, and 34th days are illustrated in Fig. 10. On August 13, 2006 (the 3rd day), the surface eddy core is located at 20.3°N and 119.7°E, and the surface eddy radius is 42.4 km (Fig. 10a). A warm water originating from the Kuroshio intrusion moves into the SCS (white curvilinear vector in Fig. 10). The counter-

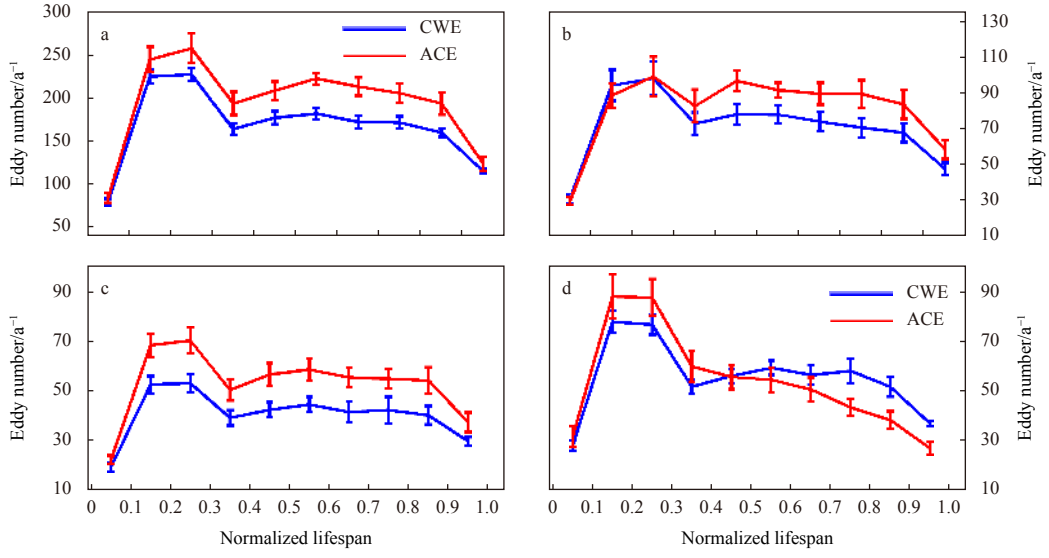

Fig. 7. Annual average number of the CWEs (blue line) and ACEs (red line) in different normalized stages in the whole SCS (a), northern SCS (b), southwestern SCS (c), and southeastern SCS (d). The standard deviations are shown as error bars.

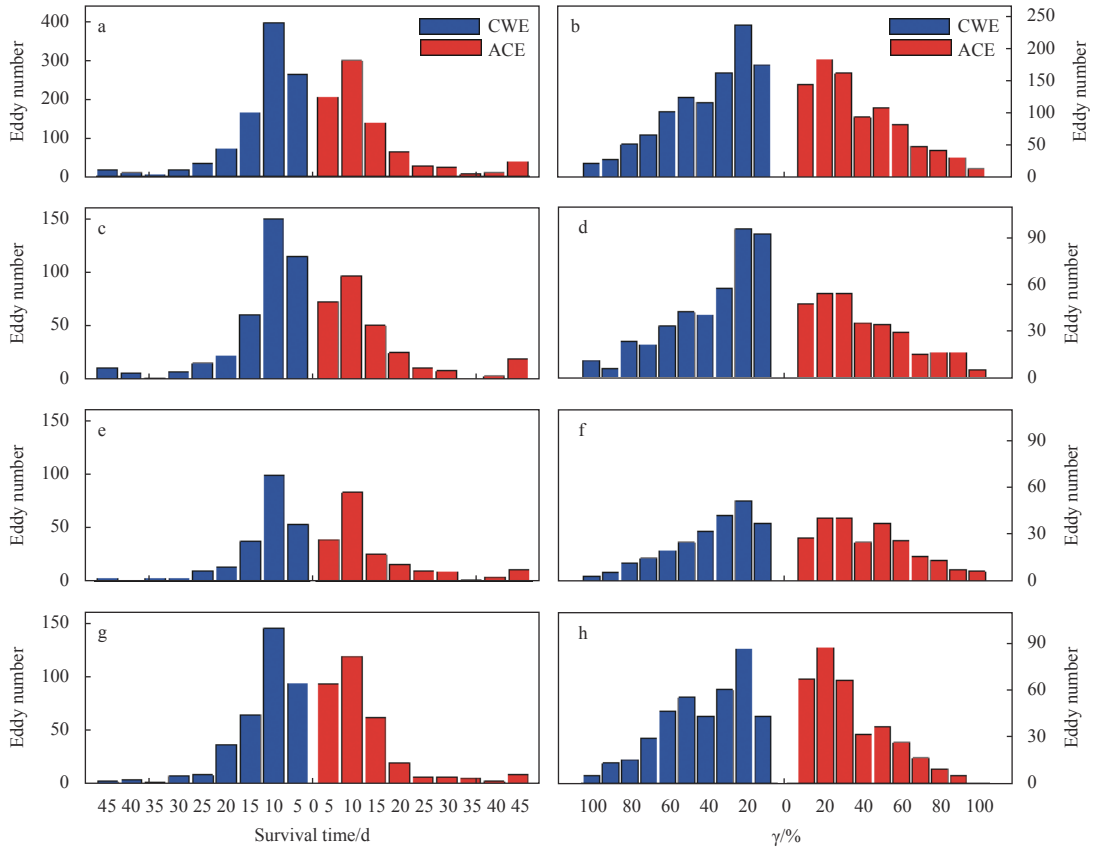

Fig. 8. Eddy survival time (left column, unit: d) and "abnormal" time-length ratio γ (right column, unit: %) for CWEs (blue bar) and ACEs (red bar) in the whole SCS (a, b), northern SCS (c, d), southwestern SCS (e, f), and southeastern SCS (g, h). Eddies with survival time longer than 40 d are all included in the 40–45 d.

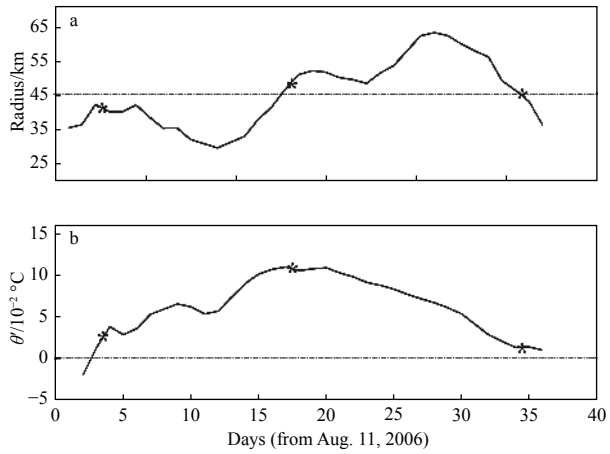

Fig. 9. Evolution of the CWE radius (a, unit: km) and potential temperature anomalies (b, unit: 10^{-2}°C). The dashed black line indicates the average radius in a and 0°C in b. The latter is used to separate the "normal" eddy (below 0°C) from the "abnormal" eddy (above 0°C). The asterisks indicate the 3rd, 17th, and 34th day, respectively.

clockwise meandering of this flow is considered the reason for the formation of the CWE. Influenced by the meandering flow, the velocity field rotates around the eddy in a counter-clockwise direction. The northern side of this CWE is warmer than the southern side.

On August 27, 2006 (the 17th day), the surface center of this CWE is still at 20.3°N, and 119.7°E, but the surface eddy radius enlarges to 46.9 km (Fig. 10b). The Kuroshio path shifts to the east and no longer intrudes into the SCS. Due to the horizontal rotation, the warm water in the northern side of the eddy (Fig. 10a) has moved to its southern side, while the relatively colder water occupies the northern side. Without the supply of the warm water from the Kuroshio, the water around the CWE gradually cools down, while the water inside the CWE is captured by this eddy and almost keeps unchanged. At this time, the potential temperature difference peaks. The inner part is warmer than the outer part by more than 0.1°C (Fig. 9b).

On September 13, 2006 (the 34th day), the surface center of the CWE moves to 20.7°N and 119.7°E, and the surface radius decreases to 46.5 km (Fig. 10c). Without the provision of the Kuroshio warm water, the background temperature around this eddy decreases, leading to a gradual decrease in θ' (Fig. 9b). Finally, this CWE disappears on September 15, 2006. In a word, the intrusion of the warm Kuroshio water changes the characteristic of the upper-layer water to form this CWE.

For the ACE case, the "abnormal" feature can persist during the whole lifespan (17 d). The evolution of the surface eddy radius and θ' is shown in Fig. 11. The surface eddy radius increases from generation to "mature" stage, then gradually decreases. The average surface eddy radius is 65.0 km, and the maximum value is 75.0 km on the 9th day of the lifespan, while the minimum value is 46.0 km on the 17th day of the lifespan (Fig. 11a). θ' is

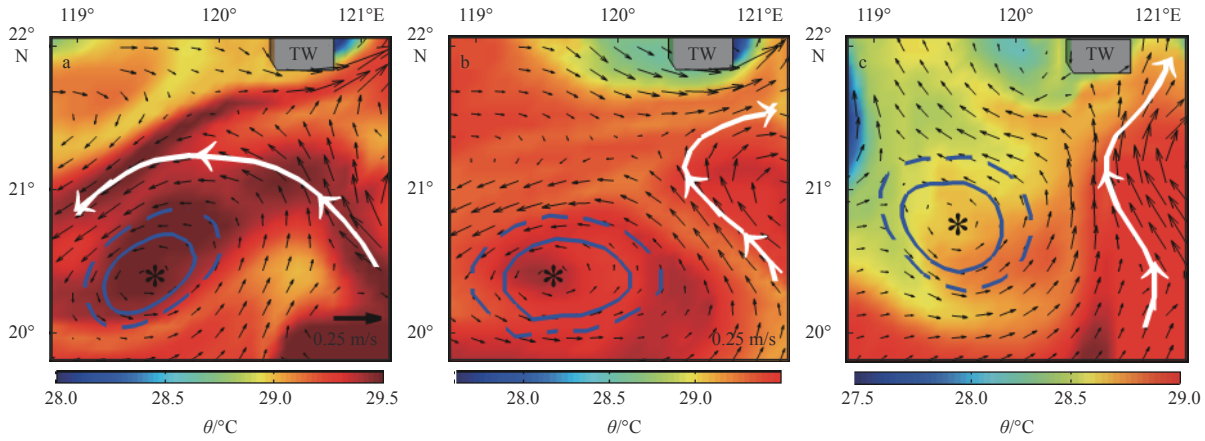

Fig. 10. Distribution of surface velocity (black vectors; unit: m/s) and SST (shadings; unit: °C) on the 3rd (a), 17th (b) and 34th day (c) for the CWE case. The blue solid and dashed contours represent the boundaries of the CWE (outermost enclosed contour of local stream function around the eddy center) and the outer boundaries of the background (1.5 times the radius of the eddy), respectively. The black asterisk marks the eddy center. The white curvilinear vector represents the rough path of the Kuroshio. TW is the abbreviation of the Taiwan Island. The velocity field is drawn at every two points.

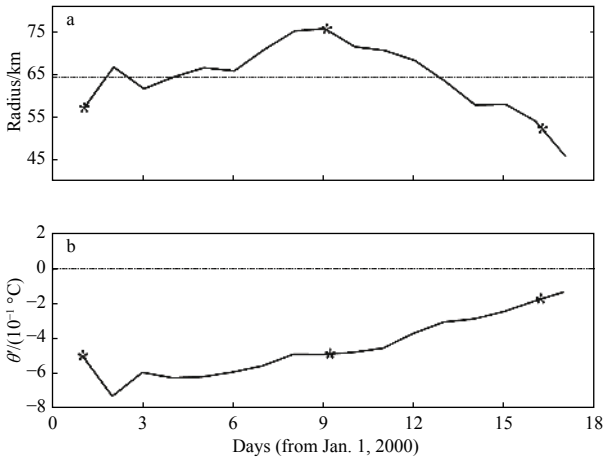

Fig. 11. Evolution of the ACE radius (a, unit: km) and potential temperature anomalies (b, unit: 10^{-1}°C). The dashed black line indicates the average radius in a and 0°C in b. The latter is used to separate the "normal" eddy (above 0°C) from the "abnormal" eddy (below 0°C). The asterisks indicate the 1st, 9th, and 16th day, respectively.

highest in the initial stage, then gradually decreases to nearly zero. The maximum amplitude of θ' is about 0.7°C, which appears on the 2nd day of the lifespan, and the minimum amplitude is 0.1°C, which appears on the 16th day of the lifespan (Fig. 11b).

To understand the generation mechanism of this ACE, the surface velocity and SST on the 1st, 9th, 16th day are displayed in Fig. 12. On January 1, 2000 (the 1st day), the intrusion of Kuroshio warm water is observed, and a relative cold-water mass is trapped in the loop (unclosed) of the Kuroshio path. Afterwards, the water mass pinches off the Kuroshio to form this eddy. This cold eddy is obviously surrounded by the warmer water from Kuroshio, except for the eastern part. During the formation stage, the potential temperature difference θ' is relatively large (–0.5°C from Fig. 11b). As the eddy develops, it is totally surrounded by the Kuroshio warm water.

On January 9, 2000 (the 9th day), the Kuroshio invasion has weakened, and the warm water entering the SCS reduces significantly (Fig. 12a). The surface radius of the ACE reaches the maximum of 75 km, and the θ' is –0.5°C (Fig. 11b). On January 16, 2000 (the 16th day), the surface eddy center moves to 21.5°N and 119.5°E, and its surface eddy radius decreases to 50.0 km. Due to the convergence effect of the anticyclone clockwise flow, the surrounding warm water is continuously captured inside of the eddy, which makes θ' decrease continuously. At this time, the Kuroshio path no longer intrudes into the SCS, and this eddy rapidly decays.

Besides the intrusion of the Kuroshio warm water, there are several other possible mechanisms. One is the instability process of the eddy. An eddy radius can suddenly enlarge in the "youth stage" or "aged stage", and thus entrap the surrounding sea water to form an "abnormal" eddy. The interaction between eddies may be another contributor (Sun et al., 2019). Similar to the eddies in the North Pacific Ocean, the mode water may also generate ACEs in the SCS, due to the strong mixing in winter (Xu et al., 2017). In a word, the CW-ACE is not an individual phenomenon, and the generation mechanism is still an ongoing and needs further research in the future.

6 Conclusions

Based on a 9-year (2000–2008) numerical model output data, this study finds a number of "abnormal" CW-ACEs in the SCS. Using the ESC method, 8 620 CWEs and 9 879 ACEs are detected from January 1, 2000 to December 31, 2008, corresponding to 14.6% and 15.8% of the total eddy number. In the vertical direction, the number of CW-ACEs decreases with depth in the whole SCS, and the CWEs are less than ACEs in the upper 200 m, while more than ACEs below 200 m. This suggests that the decreasing rate of the ACEs is larger than that of the CWEs. Most of the CW-ACEs are located to the northwest of the Luzon Strait. This may be related to the Kuroshio intrusion into the SCS, based on the case analysis. The eddy radius varies with depth and is region-dependent. The largest radius of CW-ACEs occurs at 50 m, and the average radius decreases from 50 m to 700 m. The largest CW-ACEs appear to the southeast of Vietnam in the upper 100 m, while the radius is larger in the central SCS below 200 m.

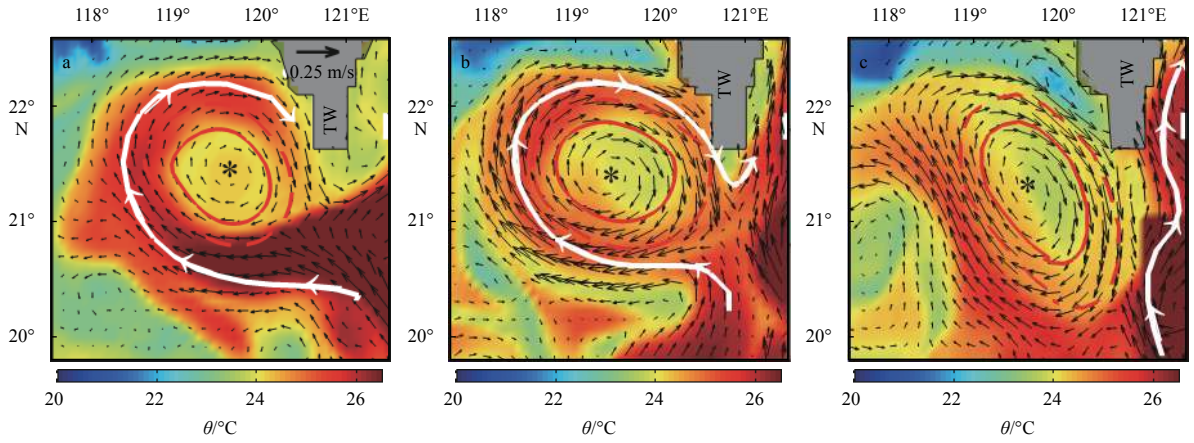

Fig. 12. Distribution of surface velocity (black vectors; unit: m/s) and SST (shadings; unit: °C) on the 1st (a), 9th (b) and 16th day (c) for the ACE case. The red solid and dashed contours represent the boundaries of the ACE (outermost enclosed contour of local stream function around the eddy center) and the outer boundaries of the background (an annular region between the eddy boundary and the circle with radius 1.5 times the radius of the eddy), respectively. The black asterisk marks the eddy center. The white curvilinear vector represents the rough path of the Kuroshio. TW is the abbreviation of the Taiwan Island. The velocity field is drawn at every two points.

In terms of the generation time, the CW-ACEs mainly occur in the early stage, about 0.1–0.3 in the normalized lifespan of the corresponding eddies. Compared with the "normal" eddies, the survival times of the "abnormal" eddies are shorter in the SCS, and this is well captured in all the three subregions. It is only about (7.8±0.3) d for CWEs and (10.8±0.9) d for the ACEs. The survival time of CWEs (ACEs) occupies 16.3% (17.1%) of the total eddy lifespan. Only a few "abnormal" eddies can persist throughout the whole lifespan. The strength of "abnormal" eddies is usually smaller than that of "normal" eddies. The temperature and salinity changes induced by "abnormal" eddies are only about 10% of those caused by "normal" eddies. The average depth of the "abnormal" θ' associated with CWEs and ACEs is 40.8 m and 40.5 m, respectively. It is a little deeper than the local mixed layer depth (33.1 m), which is defined as the depth with a temperature 0.5°C lower than the surface temperature.

In addition, the evolution of the CW-ACE cases is also discussed. A case study shows that the intrusion of the Kuroshio warm water gives rise to the CWE. With the shift of the Kuroshio path, the CWE gradually dissipates and eventually disappears as the warm water supply is cut off. The Kuroshio warm water entraps relatively cold-water mass, and the loop shedding generates the ACE. That is, the intrusion of the Kuroshio warm water into the SCS is considered as a mechanism for the formation of "abnormal" eddies. Characteristic statistics analysis of "abnormal" eddies contributes to the comprehensive understanding of the mesoscale eddy in the SCS. Demonstrating the spatial distribution of these "abnormal" eddies in the SCS provides a reference for choosing the observation areas in future work. The discussion of the CW-ACEs generation mechanism can contribute to the content of the mesoscale eddy dynamics.

Acknowledgements

The altimeter data are obtained from the AVISO Website, and the AVHRR SST product data were obtained from the NASA JPL Website. The wind forcing and lateral open boundary conditions are from the NOAA and SODA product, respectively. We thank the editor and two anonymous reviewers for their constructive comments and helpful suggestions on an earlier version of the manuscript.

References

Byrne D, Münnich M, Frenger I, et al. 2016. Mesoscale atmosphere ocean coupling enhances the transfer of wind energy into the ocean. Nature Communications, 7: ncomms11867, doi: 10.1038/ncomms11867

Chaigneau A, Gizolme A, Grados C. 2008. Mesoscale eddies off Peru in altimeter records: identification algorithms and eddy spatio-temporal patterns. Progress in Oceanography, 79(2–4): 106–119, doi: 10.1016/j.pocean.2008.10.013

Chelton D B, Gaube P, Schlax M G, et al. 2011. The influence of nonlinear mesoscale eddies on near-surface oceanic chlorophyll. Science, 334(6054): 328–332, doi: 10.1126/science.1208897

Chen Gengxin, Gan Jianping, Xie Qiang, et al. 2012. Eddy heat and salt transports in the South China Sea and their seasonal modulations. Journal of Geophysical Research: Oceans, 117(C5): C05021, doi: 10.1029/2011JC007724

Chen Gengxin, Hou Yijun, Chu Xiaoqing. 2011. Mesoscale eddies in the South China Sea: mean properties, spatiotemporal variability, and impact on thermohaline structure. Journal of Geophysical Research: Oceans, 116(C6): C06018, doi: 10.1029/2010JC006716

Chen Gengxin, Wang Dongxiao, Dong Changming, et al. 2015. Observed deep energetic eddies by seamount wake. Scientific Reports, 5: 17416, doi: 10.1038/srep17416

Chi P C, Chen Yuchun, Lu Shihua. 1998. Wind-driven South China Sea deep basin warm-core/cool-core eddies. Journal of Oceanography, 54(4): 347–360, doi: 10.1007/bf02742619

Chu Xiaoqing, Xue Huijie, Qi Yiquan, et al. 2014. An exceptional anticyclonic eddy in the South China Sea in 2010. Journal of Geophysical Research: Oceans, 119(2): 881–897, doi: 10.1002/2013JC009314

Doglioli A M, Blanke B, Speich S, et al. 2007. Tracking coherent structures in a regional ocean model with wavelet analysis: application to Cape Basin eddies. Journal of Geophysical Research: Oceans, 112(C5): C05043, doi: 10.1029/2006JC003952

Dong Changming, Lin Xiayan, Liu Yu, et al. 2012. Three-dimensional oceanic eddy analysis in the Southern California Bight from a numerical product. Journal of Geophysical Research: Oceans, 117(C7): C00H14, doi: 10.1029/2011JC007354

Dong Changming, McWilliams J C, Liu Yu, et al. 2014. Global heat and salt transports by eddy movement. Nature Communications, 5: 3294, doi: 10.1038/ncomms4294

He Qingyou, Zhan Haigang, Cai Shuqun, et al. 2016. Eddy effects on surface chlorophyll in the northern South China Sea: mechanism investigation and temporal variability analysis. Deep-Sea

Research Part I: Oceanographic Research Papers, 112: 25–36, doi: 10.1016/j.dsr.2016.03.004
He Qingyou, Zhan Haigang, Cai Shuqun, et al. 2018. A new assessment of mesoscale eddies in the South China Sea: surface features, three-dimensional structures, and thermohaline transports. Journal of Geophysical Research: Oceans, 123(7): 4906–4929, doi: 10.1029/2018JC014054
Hu Jianyu, Gan Jianping, Sun Zhenyu, et al. 2011. Observed three-dimensional structure of a cold eddy in the southwestern South China Sea. Journal of Geophysical Research: Oceans, 116(C5): C05016, doi: 10.1029/2010JC006810
Hu Jianyu, Kawamura H, Hong Huasheng, et al. 2000. A review on the currents in the South China Sea: seasonal circulation, South China Sea warm current and Kuroshio intrusion. Journal of Oceanography, 56(6): 607–624, doi: 10.1023/a:1011117531252
Itoh S, Yasuda I. 2010a. Characteristics of mesoscale eddies in the Kuroshio-Oyashio Extension region detected from the distribution of the sea surface height anomaly. Journal of Physical Oceanography, 40(5): 1018–1034, doi: 10.1175/2009JPO4265.1
Itoh S, Yasuda I. 2010b. Water mass structure of warm and cold anticyclonic eddies in the western boundary region of the Subarctic North Pacific. Journal of Physical Oceanography, 40(12): 2624–2642, doi: 10.1175/2010JPO4475.1
Ji Jinlin, Dong Changming, Zhang Biao, et al. 2017. An oceanic eddy statistical comparison using multiple observational data in the Kuroshio Extension region. Acta Oceanologica Sinica, 36(3): 1–7, doi: 10.1007/s13131-016-0882-1
Kadko D, Pickart R S, Mathis J. 2008. Age characteristics of a shelfbreak eddy in the western Arctic and implications for shelf-basin exchange. Journal of Geophysical Research: Oceans, 113(C2): C02018, doi: 10.1029/2007jc004429
Kalnay E, Kanamitsu M, Kistler R, et al. 1996. The NCEP/NCAR 40-year reanalysis project. Bulletin of the American Meteorological Society, 77(3): 437–472, doi: 10.1175/1520-0477(1996)077<0437:tnyrp>2.0.co;2
Large W G, McWilliams J C, Doney S C. 1994. Oceanic vertical mixing: a review and a model with a nonlocal boundary layer parameterization. Reviews of Geophysics, 32(4): 363–403, doi: 10.1029/94RG01872
Li Qiuyang, Sun Liang, Xu Chi. 2018. The lateral eddy viscosity derived from the decay of oceanic mesoscale eddies. Open Journal of Marine Science, 8(1): 152–172, doi: 10.4236/ojms.2018.81008
Lin Xiayan, Dong Changming, Chen Dake, et al. 2015. Three-dimensional properties of mesoscale eddies in the South China Sea based on eddy-resolving model output. Deep-Sea Research Part I: Oceanographic Research Papers, 99: 46–64, doi: 10.1016/j.dsr.2015.01.007
Liu Yu, Dong Changming, Guan Yuping, et al. 2012. Eddy analysis in the subtropical zonal band of the North Pacific Ocean. Deep-Sea Research Part I: Oceanographic Research Papers, 68: 54–67, doi: 10.1016/j.dsr.2012.06.001
Liu Yu, Dong Changming, Liu Xiaohui, et al. 2017a. Antisymmetry of oceanic eddies across the Kuroshio over a shelfbreak. Scientific Reports, 7(1): 6761, doi: 10.1038/s41598-017-07059-1
Liu Shanshan, Sun Liang, Wu Qiaoyan, et al. 2017b. The responses of cyclonic and anticyclonic eddies to typhoon forcing: the vertical temperature-salinity structure changes associated with the horizontal convergence/divergence. Journal of Geophysical Research: Oceans, 122(6): 4974–4989, doi: 10.1002/2017JC012814
Ma Jing, Xu Haiming, Dong Changming, et al. 2015. Atmospheric responses to oceanic eddies in the Kuroshio Extension region. Journal of Geophysical Research: Atmospheres, 120(13): 6313–6330, doi: 10.1002/2014JD022930
Martin A P, Richards K J. 2001. Mechanisms for vertical nutrient transport within a North Atlantic mesoscale eddy. Deep-Sea Research Part II: Topical Studies in Oceanography, 48(4–5): 757–773, doi: 10.1016/S0967-0645(00)00096-5
Mathis J T, Pickart R S, Hansell D A, et al. 2007. Eddy transport of organic carbon and nutrients from the Chukchi Shelf: impact on the upper halocline of the western Arctic Ocean. Journal of Geophysical Research: Oceans, 112(C5): C05011, doi: 10.1029/2006JC003899
McGillicuddy Jr D J. 2015. Formation of intrathermocline lenses by eddy–wind interaction. Journal of Physical Oceanography, 45(2): 606–612, doi: 10.1175/JPO-D-14-0221.1
Nan Feng, He Zhigang, Zhou Hui, et al. 2011. Three long-lived anticyclonic eddies in the northern South China Sea. Journal of Geophysical Research: Oceans, 116(C5): C05002, doi: 10.1029/2010JC006790
Nencioli F, Dong Changming, Dickey T, et al. 2010. A vector geometry-based eddy detection algorithm and its application to a high-resolution numerical model product and high-frequency radar surface velocities in the Southern California Bight. Journal of Atmospheric and Oceanic Technology, 27(3): 564–579, doi: 10.1175/2009JTECHO725.1
Pickart R S, Weingartner T J, Pratt L J, et al. 2005. Flow of winter-transformed Pacific water into the Western Arctic. Deep-Sea Research Part II: Topical Studies in Oceanography, 52(24–26): 3175–3198, doi: 10.1016/j.dsr2.2005.10.009
Qiu Chunhua, Liang Hong, Huang Yan, et al. 2020. Development of double cyclonic mesoscale eddies at around Xisha Islands observed by a 'Sea-Whale 2000' autonomous underwater vehicle. Applied Ocean Research, 101: 102270, doi: 10.1016/j.apor.2020.102270
Qiu Chunhua, Mao Huabin, Liu Hailong, et al. 2019a. Deformation of a warm eddy in the northern South China Sea. Journal of Geophysical Research: Oceans, 124(8): 5551–5564, doi: 10.1029/2019JC015288
Qiu Chunhua, Mao Huabin, Wang Yanhui, et al. 2019b. An irregularly shaped warm eddy observed by Chinese underwater gliders. Journal of Oceanography, 75(2): 139–148, doi: 10.1007/s10872-018-0490-0
Qu Tangdong. 2000. Upper-layer circulation in the South China Sea. Journal of Physical Oceanography, 30(6): 1450–1460, doi: 10.1175/1520-0485(2000)030<1450:ULCITS>2.0.CO;2
Rabinovich A B, Thomson R E, Bograd S J. 2002. Drifter observations of anticyclonic eddies near Bussol' Strait, the Kuril Islands. Journal of Oceanography, 58(5): 661–671, doi: 10.1023/A:1022890222516
Rogachev K A. 2000. Recent variability in the Pacific western subarctic boundary currents and Sea of Okhotsk. Progress in Oceanography, 47(2–4): 299–336, doi: 10.1016/S0079-6611(00)00040-9
Shchepetkin A F, McWilliams J C. 2003. A method for computing horizontal pressure-gradient force in an oceanic model with a nonaligned vertical coordinate. Journal of Geophysical Research: Oceans, 108(C3): 3090, doi: 10.1029/2001JC001047
Spall M A, Pickart R S, Fratantoni P S, et al. 2008. Western Arctic shelfbreak eddies: formation and transport. Journal of Physical Oceanography, 38(8): 1644–1668, doi: 10.1175/2007JPO3829.1
Su Danyi, Lin Pengfei, Mao Huabin, et al. 2020. Features of slope intrusion mesoscale eddies in the northern South China Sea. Journal of Geophysical Research: Oceans, 125(2): e2019JC015349, doi: 10.1029/2019JC015349
Sun Wenjin, Dong Changming, Tan Wei, et al. 2018. Vertical structure anomalies of oceanic eddies and eddy-induced transports in the South China Sea. Remote Sensing, 10(5): 795, doi: 10.3390/rs10050795
Sun Wenjin, Dong Changming, Tan Wei, et al. 2019. Statistical characteristics of cyclonic warm-core eddies and anticyclonic cold-core eddies in the North Pacific based on remote sensing data. Remote Sensing, 11(2): 208, doi: 10.3390/rs11020208
Sun Wenjin, Dong Changming, Wang Ruyun, et al. 2017. Vertical structure anomalies of oceanic eddies in the Kuroshio Extension region. Journal of Geophysical Research: Oceans, 122(2): 1476–1496, doi: 10.1002/2016JC012226
Wang Huimeng, Du Yunyan, Liang Fuyuan, et al. 2019a. A census of the 1993–2016 complex mesoscale eddy processes in the South China Sea. Water, 11(6): 1208, doi: 10.3390/w11061208
Wang Zifei, Li Qiuyang, Sun Liang, et al. 2015a. The most typical shape of oceanic mesoscale eddies from global satellite sea level observations. Frontiers of Earth Science, 9(2): 202–208,

doi: 10.1007/s11707-014-0478-z
Wang Guihua, Su Jilan, Chu P C. 2003. Mesoscale eddies in the South China Sea observed with altimeter data. Geophysical Research Letters, 30(21): 2121, doi: 10.1029/2003GL018532
Wang Qiang, Zeng Lili, Chen Ju, et al. 2020. The linkage of Kuroshio intrusion and mesoscale eddy variability in the northern South China Sea: subsurface speed maximum. Geophysical Research Letters, 47(11): e2020GL087034, doi: 10.1029/2020GL087034
Wang Qiang, Zeng Lili, Li Jian, et al. 2018. Observed cross-shelf flow induced by mesoscale eddies in the northern South China Sea. Journal of Physical Oceanography, 48(7): 1609–1628, doi: 10.1175/JPO-D-17-0180.1
Wang Qiang, Zeng Lili, Zhou Weidong, et al. 2015b. Mesoscale eddies cases study at Xisha waters in the South China Sea in 2009/2010. Journal of Geophysical Research: Oceans, 120(1): 517–532, doi: 10.1002/2014jc009814
Wang Sen, Zhu Weijun, Ma Jing, et al. 2019b. Variability of the great whirl and its impacts on atmospheric processes. Remote Sensing, 11(3): 322, doi: 10.3390/rs11030322
Wu C R, Chiang T L. 2007. Mesoscale eddies in the northern South China Sea. Deep-Sea Research Part II: Topical Studies in Oceanography, 54(14–15): 1575–1588, doi: 10.1016/j.dsr2.2007.05.008
Xian Tao, Sun Liang, Yang Yuanjian, et al. 2012. Monsoon and eddy forcing of chlorophyll-*a* variation in the northeast South China Sea. International Journal of Remote Sensing, 33(23): 7431–7443, doi: 10.1080/01431161.2012.685970
Xiu Peng, Chai Fei, Shi Lei, et al. 2010. A census of eddy activities in the South China Sea during 1993–2007. Journal of Geophysical Research: Oceans, 115(C3): C03012, doi: 10.1029/2009JC005657
Xu Lixiao, Li Peiliang, Xie Shangping, et al. 2016. Observing mesoscale eddy effects on mode-water subduction and transport in the North Pacific. Nature Communications, 7: 10505, doi: 10.1038/ncomms10505
Xu Lixiao, Xie Shangping, Liu Qinyu, et al. 2017. Evolution of the North Pacific subtropical mode water in anticyclonic eddies. Journal of Geophysical Research: Oceans, 122(12): 10118–10130, doi: 10.1002/2017JC013450
Xu Lixiao, Xie Shangping, McClean J L, et al. 2014. Mesoscale eddy effects on the subduction of North Pacific mode waters. Journal of Geophysical Research: Oceans, 119(8): 4867–4886, doi: 10.1002/2014JC009861
Yang Yikai, Wang Dongxiao, Wang Qiang, et al. 2019. Eddy-induced transport of saline Kuroshio water into the northern South China Sea. Journal of Geophysical Research: Oceans, 124(9): 6673–6687, doi: 10.1029/2018JC014847
Yang Haiyuan, Wu Lixin, Liu Hailong, et al. 2013. Eddy energy sources and sinks in the South China Sea. Journal of Geophysical Research: Oceans, 118(9): 4716–4726, doi: 10.1002/jgrc.20343
Yang Xiao, Xu Guangjun, Liu Yu, et al. 2020. Multi-Source data analysis of mesoscale eddies and their effects on surface chlorophyll in the bay of Bengal. Remote Sensing, 12(21): 3485, doi: 10.3390/rs12213485
Yang Qingxuan, Zhao Wei, Liang Xinfeng, et al. 2017. Elevated mixing in the periphery of mesoscale eddies in the South China Sea. Journal of Physical Oceanography, 47(4): 895–907, doi: 10.1175/JPO-D-16-0256.1
Yasuda I, Ito S I, Shimizu Y, et al. 2000. Cold-core anticyclonic eddies South of the Bussol' Strait in the northwestern subarctic Pacific. Journal of Physical Oceanography, 30(6): 1137–1157, doi: 10.1175/1520-0485(2000)030<1137:CCAESO>2.0.CO;2
Zhang Huaimin, Bates J J, Reynolds R W. 2006. Assessment of composite global sampling: sea surface wind speed. Geophysical Research Letters, 33(17): L17714, doi: 10.1029/2006GL027086
Zhang Yanwei, Liu Zhifei, Zhao Yulong, et al. 2014a. Mesoscale eddies transport deep-sea sediments. Scientific Reports, 4: 5937, doi: 10.1038/srep05937
Zhang Yanwei, Liu Zhifei, Zhao Yulong, et al. 2015. Effect of surface mesoscale eddies on deep-sea currents and mixing in the northeastern South China Sea. Deep-Sea Research Part II: Topical Studies in Oceanography, 122: 6–14, doi: 10.1016/j.dsr2.2015.07.007
Zhang Wenzhou, Ni Qinbiao, Xue Huijie. 2018. Composite eddy structures on both sides of the Luzon Strait and influence factors. Ocean Dynamics, 68(11): 1527–1541, doi: 10.1007/s10236-018-1207-z
Zhang Zhiwei, Tian Jiwei, Qiu Bo, et al. 2016. Observed 3D structure, generation, and dissipation of oceanic mesoscale eddies in the South China Sea. Scientific Reports, 6: 24349, doi: 10.1038/srep24349
Zhang Zhengguang, Wang Wei, Qiu Bo. 2014b. Oceanic mass transport by mesoscale eddies. Science, 345(6194): 322–324, doi: 10.1126/science.1252418
Zhang Zhengguang, Zhang Yu, Wang Wei, et al. 2013. Universal structure of mesoscale eddies in the ocean. Geophysical Research Letters, 40(14): 3677–3681, doi: 10.1002/grl.50736
Zhang Zhiwei, Zhao Wei, Qiu Bo, et al. 2017. Anticyclonic eddy sheddings from Kuroshio loop and the accompanying cyclonic eddy in the northeastern South China Sea. Journal of Physical Oceanography, 47(6): 1243–1259, doi: 10.1175/JPO-D-16-0185.1
Zhong Linhao, Hua Lijuan, Luo Dehai. 2016. The eddy–mean flow interaction and the intrusion of western boundary current into the South China Sea–type basin in an idealized model. Journal of Physical Oceanography, 46(8): 2493–2527, doi: 10.1175/JPO-D-15-0220.1